Full paper

TiC supported amorphous MnOx as highly efficient bifunctional electrocatalyst for corrosion resistant oxygen electrode of Zn-air batteries

Shidong Song [a],[**], Wanjun Li [a], Ya-Ping Deng [b], Yanli Ruan [a], Yining Zhang [b], Xuhui Qin [a], Zhongwei Chen [b],[*]

[a] School of Chemistry and Chemical Engineering, Tianjin Polytechnic University, Tianjin, 300387, China
[b] Department of Chemical Engineering, Waterloo Institute for Nanotechnology, Waterloo Institute for Sustainable Energy, University of Waterloo, 200 University Avenue West, Waterloo, ON, N2L 3G1, Canada

ABSTRACT

Zn-air batteries (ZABs) represent promising candidates for the next generation energy conversion and storage systems based on their superior features to those of lithium-ion batteries, including high theoretical energy density, low cost, and high safety. However, their further development and application is severely lagged due to the lack of high efficient and durable bifunctional oxygen electrocatalysts. The widely applied carbon-based catalysts are thermodynamically instable during battery charging. Herein, TiC supported amorphous MnO_x (a-MnO_x/TiC) is reported for the first time as electrocatalyst for the corrosion resistant oxygen electrodes of ZABs. A-MnO_x/TiC delivers a remarkable activity and stability toward both oxygen reduction reaction (ORR) and oxygen evolution reaction (OER) with a high half-wave potential (0.8 V) for ORR and a low potential (1.56 V) at 10 mA cm^{-2} for OER, which far outperforms the state of the art ORR catalyst (Pt/C) and OER catalyst (IrO$_2$), as well as the Pt/C-IrO$_2$ and a-MnO_x/C bifunctional catalysts. The excellent bifunctional activity of a-MnO_x/TiC can be attributed to the efficient synergistic effect between the active amorphous MnO_x catalyst and the highly conductive and stable TiC support. More impressively, a-MnO_x/TiC demonstrates an outstanding electrochemical stability in strong alkaline electrolyte under OER condition in contrast to the readily oxidized carbon-based a-MnO_x/C catalysts. ZAB with a-MnO_x/TiC delivers a greater discharge performance with a peak power density of 217.1 mW cm^{-2} than that of Pt/C-based ZAB, and a surpassing discharge and charge cycling performance and stability to ZABs with Pt/C-IrO$_2$ and a-MnO_x/C. Furthermore, a-MnO_x/TiC can be applied for solid-state ZABs which exhibit excellent mechanical flexibility and cycle stability under their flat and bent states. The a-MnO_x/TiC bifunctional electrocatalyst with extraordinarily high activity and electrochemical stability provides a promising approach for exploring corrosion resistant electrocatalysts for Zn-air batteries with high efficiency and long-term cycling stability.

1. Introduction

The ever-increasing environmental issues and energy demands has driven the development of energy storage systems with high energy density. Though Li-ion batteries (LIBs) has led markets ranging from portable electronics to electric vehicles (EVs) [1–3], their insufficient energy density (200–250 Wh kg^{-1}), high cost (250 US\$ kW h^{-1}), and innate safety concerns severely lag the electrification process of the society [4,5]. Rechargeable Zn-air batteries (ZABs), featuring high theoretical and actual energy density (1086 and up to 400 Wh kg^{-1},

respectively), low cost (~160 US\$ kW h^{-1}) and high safety owing to the use of nonflammable aqueous electrolytes, have been recognized as a compelling alternative to LIBs [6–8]. Furthermore, ZABs are highly versatile and suitable for the broad usage in either EVs [9] or wearable power supplies [10,11], which may employ liquid electrolytes and flexible solid-state gel electrolytes, respectively. However, their widespread application is largely impeded by the lack of stable and efficient bifunctional ORR/OER oxygen electrocatalysts due to the harsh condition under OER potentials [12,13]. As ORR and OER normally differ in reaction sites and steps on catalysts, good ORR catalyst may not perform

well for OER [14]. Accordingly, it is very challenging to achieve efficient ORR/OER bifunctional activity on a single catalyst [14]. A viable choice may be to use the hybrid catalysts composed of separate ORR catalysts and OER catalysts, such as Pt-IrO₂, in which Pt and IrO₂ only performs well for one direction of ORR and OER, respectively. Nevertheless, the large scale application of these noble metal based catalysts is limited due to their high cost and scarcity, as well as the insufficient durability during battery operation. Consequently, tremendous research efforts have been dedicated to pursue the cost-effective, highly active and robust bifunctional catalysts [15,16].

Carbon-based materials with high electronic conductivity, large specific surface area and excellent ORR activity have been extensively applied for ORR electrodes of fuel cells and metal-air batteries [17–19]. However, they are susceptible to thermodynamic instability under the oxidative OER conditions. Thermodynamically, corrosion of carbon materials can occur above 1.46 V vs. Zn^{2+}/Zn to form carbonate ions [20], as depicted in Eqn. (1) and Fig. 1a, which further forms carbonates i.e. the carbonation problem, resulting in the decrease in conductivity of electrolytes and clogging of pores in oxygen electrodes.

$$C + 6OH^- \rightarrow CO_3^{2-} + 3H_2O + 4e^- \qquad (1)$$

The external cause for carbonation problem that arises from the reaction of CO_2 in atmosphere with alkaline electrolytes can be effectively eliminated by treating the inlet air through a peripheral alkaline scrubber [21]. Nevertheless, the internal cause ascribed to carbon corrosion cannot be avoided when using the carbon-based oxygen electrodes for ZABs. In this case, the conflict between carbon-corrosion and carbon-catalysis is hardly reconcilable. The merits of carbon materials including high specific surface areas (SSAs), abundant active sites and delicate nanostructures may be gradually lost by corrosion during

OER process. Some graphitized carbon materials, like graphene and carbon nanotubes (CNT) with structures featuring sp2 orbital hybridized, are relatively stable among carbon materials and have been extensively applied as the substrates or catalysts for bifunctional oxygen electrodes [22,23]. However, their electrochemical oxidization is ultimately inevitable since the OER potential normally exceeds 1.5 V, especially at significant current densities. It is then highly desirable to explore corrosion resistant oxygen electrode materials which satisfy simultaneously sufficient electronic conductivity, high chemical and electrochemical stability, low cost, and superior ORR/OER activities relative to noble metal based catalysts.

Transition metal oxides (TMOs) have been widely investigated as corrosion resistant bifunctional electrocatalysts, such as spinel [24], perovskite [25] and other structures [26]. Nevertheless, the relatively low electronic conductivity largely confines the use of TMOs as electrocatalysts. Among TMOs, manganese oxides (MnO_x) are particularly attractive and have been explored as ORR and OER catalysts due to their rich oxidation states, various crystal structures, low cost and environmental friendliness [27–29]. Mn^{III}/Mn^{IV} redox couple can facilitate ORR via a direct four-electron reduction pathway as an oxygen acceptor-donor [30]. Meanwhile, it is also regarded to promote OER based on the oxidation of Mn^{III} to Mn^{IV} [31]. Amorphous manganese oxides (denoted as a-MnO_x) with abundant surface defects and higher Mn^{III}/Mn^{IV} content can thereby outperform some of their crystalline counterparts on the catalysis of ORR and OER [32]. For facilitating the electronic conductivity and alleviating the particle aggregation of MnO_x, highly conductive substrates are normally applied to anchor and confine the catalyst nanoparticles. Recently, carbides (WC [33], TiC [34], Mo_2C [35], B_4C [36,37], etc.) have been investigated as promising materials, either as catalysts or substrates, for corrosion resistant oxygen
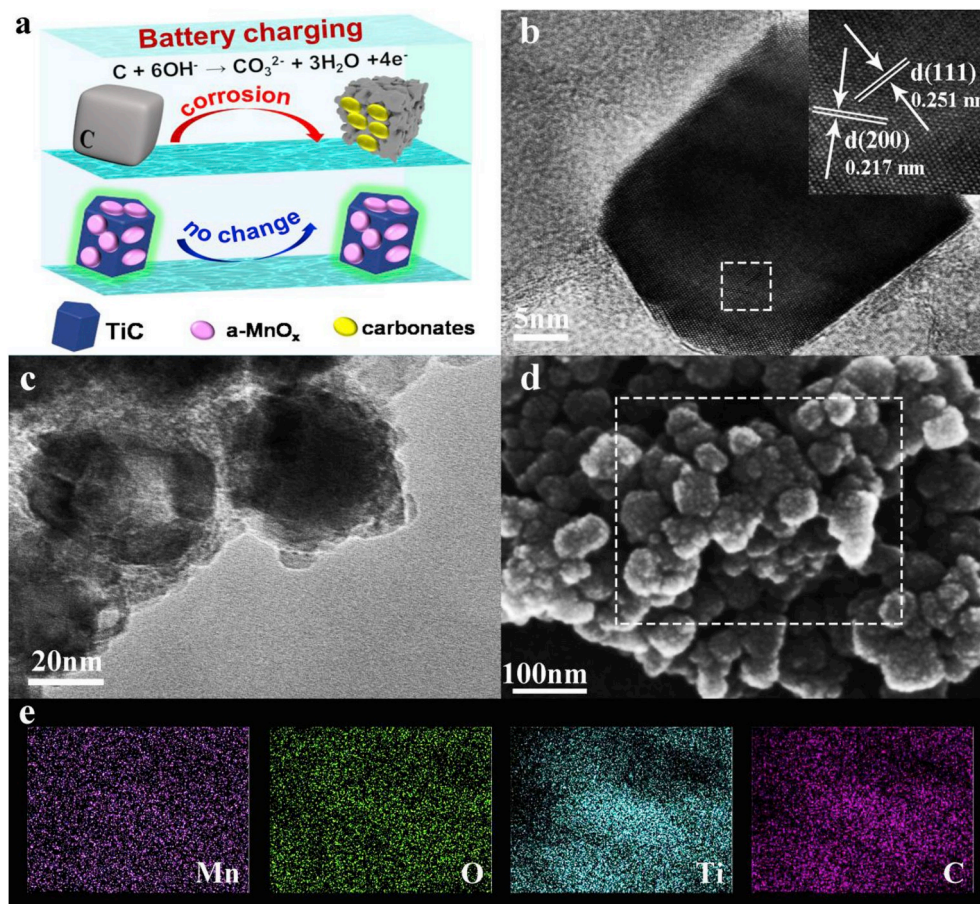
Fig. 1. Schematic diagram of carbon-based catalyst undergoing corrosion during battery charging and a-MnO_x/TiC catalyst remaining stable after charging (a); TEM images of TiC (b) and a-MnO_x/TiC NPs (c); FESEM image of a-MnO_x/TiC NPs (d) and the corresponding EDS mapping images for Mn, O, Ti and C elements (e).

electrocatalysts due to their excellent ORR/OER activity, good electronic conductivity, and high chemical and electrochemical stability. However, most of the literature references only focus on either the ORR or OER activity of carbide-based oxygen electrodes [33–36]. To the best of our knowledge, the bifunctional applications of carbide-based oxygen electrodes for rechargeable metal air batteries have been rarely seen. Among the carbides, TiC possesses high electronic conductivity ($\sim 10^4$ S cm^{-1}) and stability, making it a promising substrate for catalysts [38]. In rechargeable Li-O$_2$ batteries, TiC demonstrated significant activity and stability for ORR and OER [39]. Two-dimensional (2D) layered Ti$_3$C$_2$ also exhibited excellent activity for ORR [40] and OER [41], respectively. It is then expected that TiC-supported amorphous MnO$_x$ (denoted as a-MnO$_x$/TiC) may combine the advantages of high ORR/OER activity, electronic conductivity and stability (Fig. 1a). Here we report for the first time the application of a-MnO$_x$/TiC as a bifunctional oxygen electrocatalyst, which exhibits comparable ORR activity to Pt/C and remarkably higher OER activity than IrO$_2$. ZABs with a-MnO$_x$/TiC deliver outstanding specific power, high discharge and charge efficiency and long-term cycling stability.

2. Experimental

2.1. Materials and preparation

TiC (50 nm particle size, 99% purity) and carbon black (Vulcan XC-72R, CABOT) were commercial products purchased from Macklin Biochemical (Shanghai) and Flychem Co. (Beijing), respectively. Pt/C (20% Pt content) and IrO$_2$ (99.9% purity) were ordered from Johnson Matthey Co. and Aladdin Industrial Co., respectively. A-MnO$_x$/TiC was synthesized by depositing a-MnO$_x$ on TiC nanoparticles (NPs) via a hydrothermal synthesis method [32]. Briefly, TiC was dispersed in ethylene glycol under vigorous stirring and then pH was adjusted to ~7 by adding 0.5 M NaOH solution. After KMnO$_4$ was added and solved into the suspension, the precursor was transferred to an autoclave and heated at 70 °C for 4 h. Finally, the as-prepared a-MnO$_x$/TiC powders were washed with deionized water by repeated centrifugations and subsequently dried at 40 °C under vaccum. Carbon black (Vulcan XC-72R)-supported amorphous MnO$_x$ (denoted as a-MnO$_x$/C) and pristine a-MnO$_x$ were additionally prepared as reference materials with the same procedure, using carbon black as the substrate instead of TiC or without adding TiC support. The oxygen electrode was fabricated by catalyst (a-MnO$_x$/TiC, a-MnO$_x$/C, Pt/C or Pt/C-IrO$_2$) and Nafion binder (5%, DuPont Fluoroproducts) without electronically conductive additive or other catalyst. Briefly, catalyst particles were ultrasonically dispersed in DMF solvent with Nafion until it forms a uniform ink. The catalyst ink was then coated onto a 316 stainless steel wire gauze (500 mesh, 0.1 mm thick) to form an oxygen electrode with robust flexibility and arbitrary bending properties. The weight ratio of catalyst with Nafion is about 67:33. Typical loading of catalyst in Nafion bound electrodes was 1 mg cm^{-2}. The geometric area of oxygen electrode was about 0.5 cm^2. Water-proof gas diffusion layer (GDL) was pressed on the back of the oxygen electrode to permit O$_2$ transfer into the battery and suppress water permeation.

2.2. Electrochemical evaluation

The ORR and OER activity of oxygen electrode catalysts were investigated at room temperature using a rotating disk electrode (RDE; 3 mm in diameter) and a rotating ring-disk electrode (RRDE; 4 mm in diameter) on RRDE-3A device (ALS, Japan) connected with CHI 760E electrochemical workstation (CH Instruments, China). All the electrochemical measurements were performed in a standard 3-electrode system in 0.1 M KOH electrolyte saturated with N$_2$ or O$_2$. A Pt disk (1 cm^2) and a saturated calomel electrode (SCE) were used as the counter electrode (CE) and reference electrode (RE), respectively. For working electrode (WE), 7 μL catalyst ink as prepared in 2.1 was coated on RDE

or RRDE and dried in the air at room temperature. The catalyst loading on the WE was about 0.44 mg cm^{-2}. For ORR tests, cyclic voltammetry (CV) was conducted at a scan rate of 50 mV s^{-1} ranging from 0 to 1.2 V. *vs.* RHE and linear sweep voltammetry (LSV) was carried out at 10 mV s^{-1} under various rotation rates. While for OER tests, a scan rate of 10 mV s^{-1} and a fixed rotation rate of 1600 rpm were applied. All potentials in this work were normalized to reversible hydrogen electrode (RHE) according to the Nernst equation ($E_{RHE} = E_{SCE} + 0.0592 \times pH + E_{SCE}^{\ominus}$). The data of Tafel slope were transformed from the LSV plots. The Koutecky–Levich (K–L) equation was used to determine the electron transfer number (n) for the ORR process (Eqn. (2)).

$$\frac{1}{j} = \frac{1}{j_L} + \frac{1}{j_K} = \frac{1}{B\omega^{1/2}} + \frac{1}{j_K} \qquad B = 0.62nFC_O D^{2/3} \nu^{-1/6} \qquad (2)$$

where j is the measured current density, j_k is the kinetic current, ω is the electrode rotation rate in rpm, F is the Faraday constant (96485 C mol^{-1}), C_o is the bulk concentration of O$_2$ (1.2×10^{-6} mol cm^{-3} in 0.1 M KOH), D_o is the diffusion coefficient of O$_2$ (1.9×10^{-5} cm^2 s^{-1} in 0.1 M KOH), and ν is the kinetic viscosity of electrolyte (0.01 cm^2 s^{-1} for 0.1 M KOH).

The peroxide yields (HO$_2^-$%) and n are calculated with the following Eqn. (3).

$$HO_2^- \% = \frac{200 i_r}{N(i_d + \frac{i_r}{N})} \qquad n = \frac{4 i_d}{i_d + \frac{i_r}{N}} \qquad (3)$$

where I_d is the disk current, I_r is the ring current, and N is the current collection efficiency of the Pt ring (0.42).

Electrochemical active surface area (ECSA) was determined by measuring the dependence of the capacitive current that arises from double-layer charging on the scan rate of CV within a potential window of 0.95–1.05 V *vs.* RHE and a scan rate range from 20 to 100 mV s^{-1}. By linear fitting the correlation between the charging current density difference ($\Delta j = j_a - j_c$) at 1.00 V *vs.* RHE and the scan rate, the slope was obtained to represent ECSA. The stability tests were conducted by recording the current density attenuation at a constant potential of 0.7 V for 12000 s at 1600 rpm in O$_2$-saturated electrolyte.

2.3. ZAB tests

ZABs were tested in a home-made electrochemical cell using 6 M KOH with 0.2 M Zn(Ac)$_2$ mixed solution as the liquid electrolyte, zinc foil as the anode and the flexible oxygen electrode as the cathode. Polarization curves and electrochemical impedance spectroscopy (EIS) were measured on CHI 760E electrochemical workstation. All impedance data were collected in the frequency range of 1 MHz to 0.1 Hz at open circuit voltage (OCV). Discharge/charge cycling performance was tested by Lanhe battery tester. Galvanostatic charging tests were performed to assess the electrochemical stability of a-MnO$_x$/TiC electrode in comparison with electrodes using a-MnO$_x$/C, Vulcan XC-72R carbon black and commercial Pt/C, respectively. ZABs with the oxygen electrodes were separately charged at a constant current density of 10 mA cm^{-2} for 24 h. After charging, the electrolyte solutions and oxygen electrodes were carefully removed for post-mortem analysis.

Foldable solid-state ZABs (SSZABs) were further assembled and tested at their flat and bent states with the same Zn anodes and oxygen electrodes as those applied in liquid ZABs, and specially prepared gel polymer-based solid electrolytes instead of liquid electrolytes. The SSZABs were sealed and wrapped using transparent acrylic tapes with small holes pierced at the oxygen electrode side as the air inlet. To prepare the solid electrolyte, PVA with a small quantity of PEO was dissolved into H$_2$O at room temperature and subsequently heated up to 90 °C. After thoroughly stirring, a transparent gel was formed. An appropriate amount of 6 M KOH with 0.2 M Zn(Ac)$_2$ mixed solution was transferred into the gel and stirred until uniform. After that, the alkaline gel was freezed and then dried to form the solid electrolyte.

2.4. Characterizations

X-ray diffraction (XRD) was performed on a Rigaku D/max-2500 X-ray diffractometer using Cu Kα radiation. The morphology and microstructure of the catalysts and electrodes were examined by a transmission electron microscope (TEM; JEOL JEM-2100) and a field-emission scanning electromicroscope (FESEM; ZEISS Gemini SEM500). Energy Dispersive X-ray Spectroscopy (EDS) analysis was conducted on a EDAX OCTANE SUPER to indicate the carbonates in SEM images. Scanning Transmission Electron Microscopy (STEM) with electron energy loss spectroscopy (EELS) were acquired using a Tecnai G^2 F20 S-TWIN microscope, equipped with a Gatan Tridiem 863 energy filter. X-ray photoelectron spectroscopy (XPS) measurements were performed with a Thermofisher K-alpha. Raman spectra were recorded with a XploRA PLUS Raman spectrometer (Horiba). Nitrogen adsorption-desorption measurements were conducted on an Micromeritics analyzer (ASAP 2020 PLUS HD88) and the specific surface areas (SSA) were determined by Brunauer-Emmett-Teller (BET) method.

3. Results and discussion

3.1. Characterization of a-MnOx/TiC

The morphology and structure of TiC and a-MnOx/TiC were examined by TEM and SEM. As shown in Fig. 1b and Fig. S1a, TiC particle is well crystallized with a size of 50 nm. The (111) and (200) plane of TiC is identified by clear lattice fringes of 0.251 and 0.217 nm, respectively. In Fig. 1c it shows a-MnOx NPs entirely cover the TiC support and the contact between a-MnOx and TiC particles appears tight, which is beneficial for the implementation of their interaction and synergistic effect. A-MnOx NPs basically have ellipsoidal shapes with particle size of about 4 nm. Pure a-MnOx NPs are additionally prepared using the same hydrothermal procedure but without adding TiC supports and then examined by high-resolution TEM (HRTEM) and XRD techniques. As shown in Fig. S1b, the selected area electron diffraction (SAED) pattern of a-MnOx shows broad rings, suggesting the amorphous state of the MnOx NPs. Furthermore, no lattice fringes can be observed in the HRTEM image. Only a small hump appears in the XRD pattern of a-MnOx sample (Fig. S2), further manifesting the as-prepared MnOx NPs are amorphous. The XRD pattern of a-MnOx/C sample in Fig. S2 also validates the amorphous character of MnOx in a-MnOx/C as it only presents two diffraction peaks at 24.9° and 43.8°, respectively related to the Vulcan XC-72R carbon black. The amorphous phase may have high density surface defects and energetic surface MnIII and MnIV ions, which can offer sufficient active sites for oxygen adsorption/desorption in ORR and OER [14,32]. Fig. 1d shows that TiC particles are packed uniformly by a-MnOx NPs, presenting a TiC-core and a-MnOx-shell structure, which can facilitate the oxygen activation processes and the charge transfer process. EDS elemental mapping images corresponding to the square area in Fig. 1d clearly present that the a-MnOx/TiC NPs have a homogeneous structure with well-dispersed a-MnOx and TiC (Fig. 1e). The N2 adsorption-desorption isotherms for TiC and a-MnOx/TiC samples are shown in Fig. S3 and can be identified as IV-type isotherm, showing characteristics of mesoporous materials. The Brunauer–Emmett–Teller (BET) specific surface areas (SSAs) of TiC and a-MnOx/TiC are 22.99 and 23.73 $m^2 g^{-1}$, respectively, indicating that the SSA of a-MnOx/TiC hybrid material is mainly determined by the TiC substrate. The pore size distribution as determined by the Barrett-Joynes-Halenda (BJH) method, shows monodispersity of pores ranging from 10 to 100 nm and peaked at 50 nm for the TiC sample, which is likely attributed to the interparticle spaces. In contrast, the a-MnOx/TiC sample exhibits a hierarchical pore structure, additionally containing a number of pores less than 4 nm, presumably owing to the spaces among a-MnOx NPs. The micropores and mesopores in a-MnOx/TiC particles may promote the oxygen trapping and diffusion at active sites for ORR and OER.

The XRD pattern of a-MnOx/TiC sample in Fig. 2a only shows the diffraction peaks of TiC (PDF#32–1083) and no distinct peak related to MnOx, suggesting the MnOx catalysts on TiC are amorphous. XPS measurements were performed for the a-MnOx/TiC sample to reveal the chemical composition and valence state. Spectrum deconvolutions of each species are carried out to show the existence of different chemical states. The fully scanned XPS spectrum of a-MnOx/TiC in Fig. 2b reveals that the sample consists of Mn, O, Ti and C. The high-resolution XPS spectra of Mn 2p apparently show two characteristic peaks with binding energies at 653.3 and 641.4 eV that corresponds to the spin doublet of Mn $2p_{1/2}$ and Mn $2p_{3/2}$, respectively (Fig. 2c). The broad shake-up satellite peak at 647.2 eV and the deconvolution of Mn $2p_{3/2}$ peak reveal the presence of mixed valence of Mn on a-MnOx surface. The peaks at 640.6, 641.6 and 643.2 eV correspond to MnII [42], MnIII [43], and MnIV [44], respectively. It is worth noting that the concomitant MnIII/MnIV couples have been recognized as crucial to the electrochemical catalysis process of both ORR and OER. In Fig. 2d, Ti 2p spectrum is deconvoluted into two sets of doublet peaks, of which one comprising two main peaks at 460.8 and 454.8 eV corresponds to Ti-C $2p_{1/2}$ and Ti-C $2p_{3/2}$, respectively. Notably, the shoulder peak located at 455.7 eV is attributable to Ti-O-C that implies the strong interaction between TiC and a-MnOx [39]. The peaks at 464.0 and 458.3 eV are separately ascribed to Ti-O $2p_{1/2}$ and Ti-O $2p_{3/2}$. The small shoulder peak at 457.8 eV indicates the existence of Ti ions with lower valences in surface Ti-suboxides which possess a good electronic conductivity of ~10^2 S cm^{-1} and can be applied as a corrosion resistant support for bifunctional electrocatalysts for metal-air batteries [39]. The O 1s spectrum shows a main peak at 529.6 eV that corresponds to Mn-O bonds (Fig. 2e). The shoulder peak at 530.7 eV is attributed to the oxygen from Ti-O-C bonds [45]. Other shoulder peaks at 532.0 and 533.2 eV are generally related to surface adsorbed oxygen species and water, respectively. The C 1s spectrum in Fig. 2f presents two peaks centered at 281.6 and 284.8 eV, related to the C-Ti and C-C bonds, respectively. A small peak at 286.0 eV arises from C-O bonds.

EELS was applied to provide the micro-region states and electronic properties of Mn and Ti in a-MnOx/TiC. In the inset of Fig. 2g, the Mn $L_{2,3}$-edge spectra acquired along the direction of arrow give the energy loss change from the core region of a-MnOx to the interface of a-MnOx and TiC. The L_3 edges present a slight shift to the higher energy loss, indicating the interaction between a-MnOx and TiC substrate. Fig. 2h shows the respective Mn $L_{2,3}$-edge spectrum which consists of two white lines L_3 and L_2. The L_3 line appears to be composed of two peaks, probably due to the existence of Mn^{3+} and Mn^{4+} [46]. The ratio of the integrated intensities of the L_3 and L_2 white lines, expressed as $I(L_3)/I(L_2)$, can be correlated to the valence of Mn in a-MnOx. The formation of oxygen vacancy is usually accompanied with the reduction of surrounding Mn ions. Mn $L_{2,3}$ white line ratio is approximately 2.3, indicating the valence of Mn primarily comprises +3 and +4 [47]. The branching ratio defined as $I(L_3)/(I(L_2) + I(L_3))$ is further calculated as 0.7, which corresponds to a mean valence state of about 3.7 for Mn [48]. The respective Ti $L_{2,3}$-edge spectrum in Fig. 2i shows the lower energy Ti L_3 and higher energy Ti L_2 edges, which is consistent with TiC phase [49]. The distinct splitting of the lower energy loss of Ti L_3 and peaks broadening is attributed to resonance scattering within the shells of the neighboring atoms [50]. Fig. S4 shows the Raman spectra for a-MnOx/TiC with TiC as the reference material. The Raman spectra for TiC show three peaks at approximately 260, 419 and 605 cm^{-1}, which are in good agreement with formerly published results [51]. Raman peaks in the acoustic range have been thought to be mainly determined by the vibrations of the heavy Ti ions, typically 150-300 cm^{-1} (LA and TA modes), whereas peaks in the optic range (400-650 cm^{-1}) have been attributed to the lighter C ions (LO and TO modes). For a-MnOx/TiC, the Raman spectra only present three peaks which correspond to TiC. No peak was clearly observed for the MnOx sample, which is in accord with its amorphous phase in the XRD pattern (Fig. 2a and Fig. S2). It is observed that after TiC is modified by a-MnOx, the Raman peaks for TiC slightly shift to higher frequencies. This frequency shift indicates the
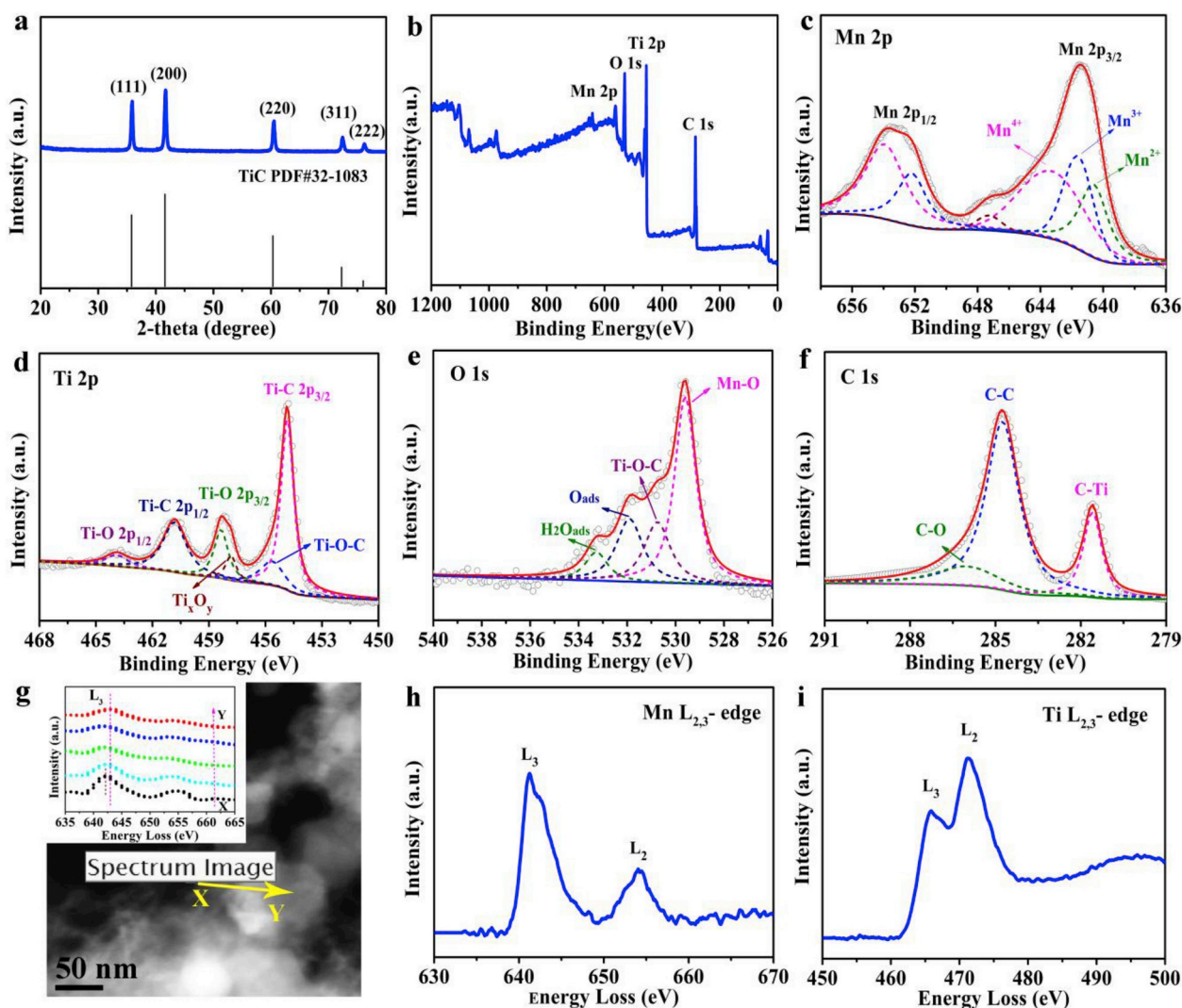
Fig. 2. XRD pattern (a) and XPS full spectrum (b) for a-MnO$_x$/TiC; XPS high-resolution spectra of Mn 2p (c), Ti 2p (d), O 1s (e) and C 1s (f); EELS spectra of a-MnO$_x$/TiC: (g) STEM image. The inset shows the multispot scanning of Mn L$_{2,3}$-edge spectra along the direction of arrow; Respective Mn L$_{2,3}$-edge (h) and Ti L$_{2,3}$-edge (i) EELS spectrum.

interaction between a-MnO$_x$ and TiC, as the coverage of a-MnO$_x$ may incur the contraction in chemical bonds for TiC.

3.2. Electrocatalytic properties toward the ORR and OER

Cyclic voltammetry (CV) was first conducted to investigate the ORR performance for a-MnO$_x$/TiC in 0.1 M KOH at a scan rate of 50 mV s^{-1} (Fig. S5). A-MnO$_x$/TiC demonstrates obvious ORR peak centered at 0.69 V in the O$_2$ saturated electrolyte, and no any redox peaks in the N$_2$ saturated electrolyte, confirming the ORR catalytic activity of a-MnO$_x$/TiC. The catalytic activities of a-MnO$_x$/TiC, Pt/C and IrO$_2$ catalysts towards both ORR and OER were systematically evaluated in O$_2$-saturated 0.1 M KOH using linear sweep voltammetry (LSV) at a sweep rate of 10 mV s^{-1} on rotating disk electrode (RDE) and rotating ring-disk electrode (RRDE). All potential values given for ORR/OER are referenced to the reversible hydrogen electrode (RHE). Pt/C and IrO$_2$ were employed as the benchmark ORR and OER electrocatalyst, respectively. As shown in Fig. 3a, LSV polarization curves performed at 1600 rpm on RDE reveal the outstanding ORR activity for a-MnO$_x$/TiC, which exhibits the same onset potential E_{onset} (0.96 V) and close limiting current density and half-wave potential $E_{1/2}$ (0.8 V) as Pt/C. Pristine a-MnO$_x$ and TiC exhibit $E_{1/2}$ of 0.50 and 0.63 V, respectively, much lower than that of a-MnO$_x$/TiC. The relatively insufficient electronic conductivity and catalytic activity

may separately limits the ORR performance of a-MnO$_x$ and TiC. However, the combination of them in a TiC-core and a-MnO$_x$-shell structure can compensate their respective weakness and further modulate their synergetic features via strong interaction. A-MnO$_x$/C performs worse than a-MnO$_x$/TiC, showing a E_{onset} of 0.88 V and $E_{1/2}$ of 0.71 V, which further indicates that the ORR activity of catalysts highly depend on the properties such as electronic conductivity and stability of substrates, as well as their interaction. The good ORR activity for TiC may contribute to attaining a high $E_{1/2}$ for a-MnO$_x$/TiC. In terms of $E_{1/2}$, a-MnO$_x$/TiC surpasses most non-precious metal electrocatalysts reported in literatures, including many carbon-based catalysts with high SSAs (Table S1). ECSAs of a-MnO$_x$/TiC and Pt/C were evaluated using the electrochemical double-layer capacitances (C_{dl}) based on the CV curves in Figs. S6a and b, respectively. Fig. S6c exhibits Pt/C has a much higher C_{dl} of 8.8 mF cm^{-2}, which is 2.8 times as that of a-MnO$_x$/TiC electrode (3.2 mF cm^{-2}), indicating the former catalyst possesses larger active surface area. Moreover, considering the large BET SSA (about 107 m^2 g^{-1}) of Pt/C in contrast to that of a-MnO$_x$/TiC catalyst (23.73 m^2 g^{-1}), the comparable ORR activity delivered by both catalysts implies a high efficiency of active sites on a-MnO$_x$/TiC due to the decent synergistic effect. Tafel plots in Fig. 3b further illustrate that Pt/C and a-MnO$_x$/TiC have similar slopes of 71.4 and 72 mV dec^{-1}, respectively, indicating their comparably fast ORR kinetics. LSV curves of ORR at different
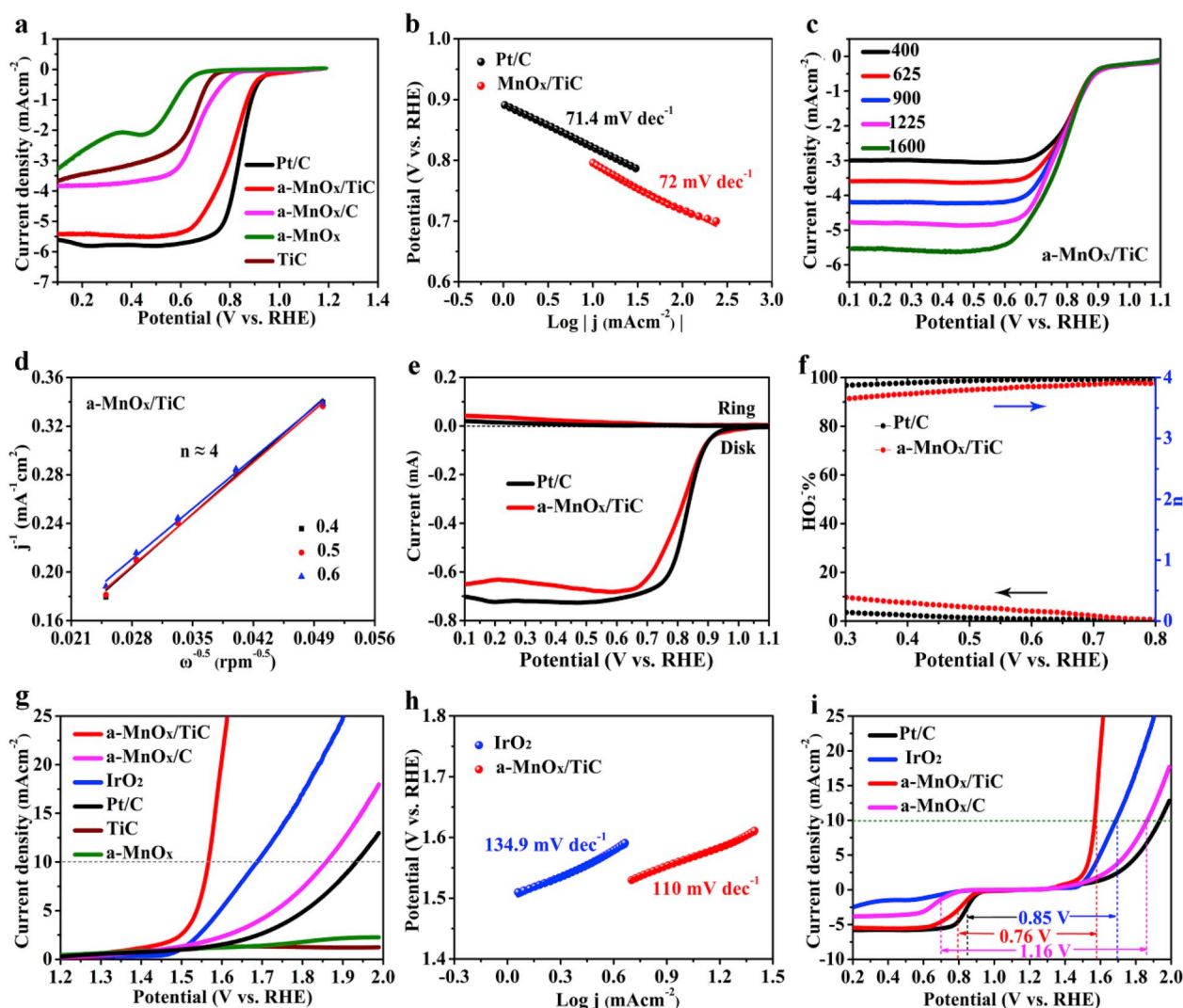
Fig. 3. LSV curves of ORR of various catalysts at 1600 rpm (a); Tafel plots obtained from LSV curves in (a) for Pt/C and a-MnO$_x$/TiC (b); LSV curves of ORR at different rotation rate of a-MnO$_x$/TiC (c); K–L plots of a-MnO$_x$/TiC (d); Linear voltammograms of a-MnO$_x$/TiC measured using RRDE (e); n and HO$_2^-$% obtained from RRDE (f); LSV curves of OER of various catalysts at 1600 rpm (g); Tafel plots obtained from LSV curves in (g) for IrO$_2$ and a-MnO$_x$/TiC (h); LSV curves of both ORR and OER for various catalysts (i).

rotation rate were conducted on RDE to explore the ORR kinetics of a-MnO$_x$/TiC. In Fig. 3c, a-MnO$_x$/TiC appears close current densities to Pt/C (see Fig. S7a) at different speeds. The electron transfer numbers (n) were calculated from the Koutechy–Levich (K–L) plots at three different potentials based on LSV curves of a-MnO$_x$/TiC and Pt/C in Fig. 3c and Fig. S7a, respectively. The K–L plot (Fig. 3d) of a-MnO$_x$/TiC presents good linearity and consistency for the three potentials, similar as that of Pt/C (Fig. S7b). The average n values for both a-MnO$_x$/TiC and Pt/C are approximately 4.0 per oxygen molecule, indicating that a-MnO$_x$/TiC as a non-noble metal catalyst has a desirable selectivity for the efficient four-electron dominated ORR pathway as the benchmark Pt/C catalyst possesses. The rotating ring disk electrode (RRDE) was employed to evidence the ORR pathways for a-MnO$_x$/TiC in comparison with Pt/C. The RRDE results in Fig. 3e exhibit the comparably disk and ring currents for a-MnO$_x$/TiC and Pt/C. Fig. 3f shows that a-MnO$_x$/TiC has high selectivity for the ORR process with electron transfer numbers of 3.66–3.96 and HO$_2^-$ yields below 9.5% in the scanning potential range of 0.3–0.8 V, quite close to those for Pt/C. The activity and stability of oxygen electrode catalysts for OER directly affect the charge-discharge efficiency and cycle life of ZABs. As shown in Fig. 3g, a-MnO$_x$/TiC delivers the lowest E_{onset} (1.45 V) and OER potential at 10 mA cm^{-2} $E_{j=10}$ (1.56 V), remarkably surpassing the benchmark IrO$_2$ catalyst with an

E_{onset} of 1.46 V and $E_{j=10}$ of 1.70 V. Both pristine a-MnO$_x$ and TiC exhibit poor OER activity, owing to the low electronic conductivity and OER activity for a-MnO$_x$ and TiC, respectively. The superior OER activity of a-MnO$_x$/TiC is among the best ones ever reported (Table S1), probably contributed from the oxidation of Mn^{III} to Mn^{IV} and the synergistic effect between a-MnO$_x$ and TiC. A-MnO$_x$/C presents a poorer OER activity ($E_{j=10}$ = 1.86 V) than a-MnO$_x$/TiC and IrO$_2$ because of the corrosion of carbon substrate, which is in accordance with the ORR activity in Fig. 3a. Pt/C only shows low OER activity with a high E_{onset} of 1.60 V and a $E_{j=10}$ of 2.0 V. The relatively lower OER Tafel slope of a-MnO$_x$/TiC (110 mV dec^{-1}) than that of IrO$_2$ (134.9 mV dec^{-1}) further demonstrates the outstanding OER activity for a-MnO$_x$/TiC (Fig. 3h). The potential gap ΔE between $E_{j=10}$ and $E_{1/2}$ is applied to comprehensively assess the bifunctional activity of oxygen electrode catalysts, as shown in Fig. 3i. A-MnO$_x$/TiC presents the lowest ΔE of 0.76 V, in contrast to Pt/C, IrO$_2$ and a-MnO$_x$/C with ΔE of 1 V, 1.01 V and 1.16 V, respectively, meaning that a-MnO$_x$/TiC has a strikingly high ORR/OER bifunctional activity and can be a promising reversible oxygen catalyst. Even based on the $E_{1/2}$ value of Pt/C (0.85 V) and $E_{j=10}$ value of IrO$_2$ (1.70 V), the ΔE value calculated is 0.85 V, still substantially higher than that of a-MnO$_x$/TiC. As shown in Table S1, a-MnO$_x$/TiC possesses comparable or higher bifunctional activity than that of the most active electrocatalysts

reported so far. This result indicate that the strong interaction of TiC substrate and a-MnOx catalyst can effectively compensate the electronic conductivity of a-MnOx, facilitate the charge transfer during ORR and OER, regulate the adsorption/desorption process of oxygen-related intermediates, and as a result, promote the ORR and OER reaction kinetics. In addition, the stable TiC can also sustain a stable structure to support and confine the a-MnOx catalyst.
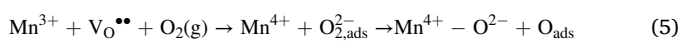
The outstanding ORR and OER activity of a-MnOx/TiC can be attributed to the synergetic effect between a-MnOx catalyst and TiC substrate, which possibly comprises the following speculations. First, the amorphous MnOx catalyst inherently possesses good capability of oxygen adsorption/desorption owing to its abundant defect sites and Mn ions with mixed valence [14,32]. Meanwhile, TiC instinctively has a high conductivity, which can serve a-MnOx a fast charge transfer process. Besides, TiC can also contribute to the catalysis of ORR and OER. Second, the strong interaction between a-MnOx and TiC, as revealed by EELS, XPS and Raman, can effectively modify the local electronic structure and accordingly induce the electron transfer between TiC and a-MnOx (Fig. 2g). Third, the modification of electronic structure can further regulate the adsorption/desorption energy and process of oxygen-related intermediates (such as O*, OH*, OOH*) [6,22], thereby facilitates the ORR and OER process to achieve a four-electron dominated pathway. The possible reaction mechanisms for ORR and OER on a-MnOx/TiC are suggested in steps (4–12), according to the related literature reports [14,46].

The formation and annihilation of oxygen vacancy, oxygen conversion, and the reduction of adsorbed oxygen are as follows [46].
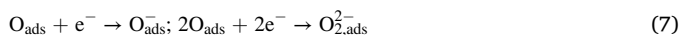
Oxygen vacancy formation:

$$Mn^{4+} - O^{2-} \rightarrow Mn^{3+} + V_O^{\bullet\bullet} + 1/2O_2(g) \tag{4}$$
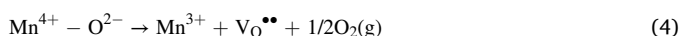
Oxygen vacancy annihilation:

$$Mn^{3+} + V_O^{\bullet\bullet} + O_2(g) \rightarrow Mn^{4+} + O_{2,ads}^{2-} \rightarrow Mn^{4+} - O^{2-} + O_{ads} \tag{5}$$
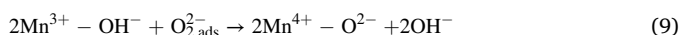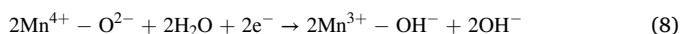
The conversion between gaseous oxygen and surface adsorbed oxygen by oxygen vacancy:

$$V_O^{\bullet\bullet} + 1/2O_2(g) + 2e^- \rightarrow O_{ads} \tag{6}$$

The reduction of adsorbed oxygen:

$$O_{ads} + e^- \rightarrow O_{ads}^-; \ 2O_{ads} + 2e^- \rightarrow O_{2,ads}^{2-} \tag{7}$$

The reaction pathway of ORR [14]:

$$2Mn^{4+} - O^{2-} + 2H_2O + 2e^- \rightarrow 2Mn^{3+} - OH^- + 2OH^- \tag{8}$$

$$2Mn^{3+} - OH^- + O_{2,ads}^{2-} \rightarrow 2Mn^{4+} - O^{2-} + 2OH^- \tag{9}$$

The reaction pathway of OER [14]:

$$Mn^{4+} - O^{2-} + OH^- \rightarrow Mn^{3+} - O - OH^- + e^- \tag{10}$$

$$Mn^{3+} - O - OH^- + OH^- \rightarrow Mn^{4+} - O - O^{2-} + H_2O + e^- \tag{11}$$

$$2Mn^{4+} - O - O^{2-} \rightarrow 2Mn^{4+} - O^{2-} + O_2 \tag{12}$$
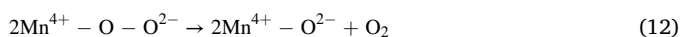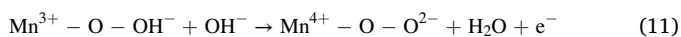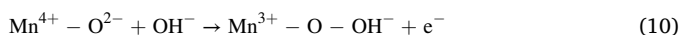
$V_O^{\bullet\bullet}$ represents the oxygen vacancy on a-MnOx. O_{ads} represents the adsorbed oxygen. On a-MnOx, the formation of oxygen vacancy is accompanied with the reduction of surrounding Mn^{4+}. The rich Mn^{3+} and Mn^{4+} ions, and oxygen vacancies can facilitate the oxygen adsorption/desorption and conversion processes, and thereby activate the ORR and OER. TiC may mainly assist the electron transfer for the active sites on a-MnOx and additionally contribute to ORR and OER.

3.3. Stability study

The chemical stability of a-MnOx/TiC in alkaline electrolyte is evaluated by soaking a-MnOx/TiC particles in 6 M KOH solution for two weeks. The structure of a-MnOx/TiC before and after test were checked by XRD. Fig. S8 shows that there is no obvious change in the XRD patterns for the a-MnOx/TiC sample before and after aging test, which indicates that a-MnOx/TiC is adequately stable in strong alkaline solution. The electrochemical stability of a-MnOx/TiC was first investigated using chronoamperometry method by a RDE system at a constant potential of 0.7 V and a fixed rotation rate of 1600 rpm. As shown in Fig. S9, after continuous ORR test for 12000 s, a-MnOx/TiC exhibits an overwhelmingly high durability with a current drop of only 5%, far lower than that for Pt/C (15%) and a-MnOx/C (44%).

All the oxygen electrodes were fabricated in a flexible style on stainless steel wire gauzes and respectively evaluated in the home-made liquid ZABs, solid-state coin cells and solid-state foldable ZABs. For practical application, the electrochemical stability of a-MnOx/TiC electrode was systematically assessed in the home-made ZABs using 6 M KOH with 0.2 M Zn(Ac)₂ mixed solution as the liquid electrolyte in contrast to a-MnOx/C electrode. ZABs were directly charged at 10 mA cm⁻² for 24 h without discharge in advance. In Fig. 4a, the charge voltage profile of a-MnOx/TiC-based ZAB shows a rise in charge voltage in a short time and then maintains consistent at 1.91 V until the end of test. ZAB with a-MnOx/C delivers obviously higher charge voltage than its a-MnOx/TiC-based counterpart for all the charge time. In addition, the charge voltage profile presents two plateaus at 1.99 V and 2.21 V, respectively, which suggests the degradation of a-MnOx/C electrode after only about 6 h. The electrolyte solution collected from the ZAB with a-MnOx/TiC after charging retains transparent, clear and colorless, as shown in Fig. 4b, manifesting the high stability of a-MnOx/TiC oxygen electrode against electrochemical oxidation. In contrast, Fig. 4c shows the electrolyte solution in ZAB with a-MnOx/C turns brown after charging, which represents a severe oxidation of carbon substrate material in a-MnOx/C oxygen electrode during OER process. A ZAB with oxygen electrode specially prepared by the commercial Vulcan XC-72R carbon black which is the same material as the carbon support of a-MnOx/C and commercial Pt/C catalyst, was additionally tested under the same condition. After charging, the electrolyte solution becomes similar brown as that for a-MnOx/C-based ZAB (Fig. S10), further confirming the change in color of electrolyte can be ascribed to the electrochemical oxidation of carbon support of a-MnOx/C. The oxidation of carbon can cause the formation of carbonate ions as well as the carboxylic acids, such as mellitic acid and humic acid, which can dissolve into the alkaline electrolyte and present a brown color [52]. The a-MnOx/TiC and a-MnOx/C oxygen electrodes were removed and gently washed by entirely dehydrated ethanol which was pre-treated using 3A molecular sieves.

SEM observation was performed for the a-MnOx/C electrode before and after galvanostatic charging test. As shown in Fig. S11a, the surface of before-testing a-MnOx/C electrode presents a typical structure for Nafion-bound electrodes with hierarchical porous. After continuous charging for 24 h, the electrode surface is packed by a solid film which is composed of overlapped microsheets (Fig. S11b). Fig. 4d further reveals that the solid film contains K, C, and O elements, indicating the existence of potassium carbonates or potassium bicarbonates. XRD spectra were subsequently conducted to characterize the after-charging a-MnOx/C and a-MnOx/TiC electrodes in contrast with their before-testing counterparts. In Fig. 4e, the XRD patterns for a-MnOx/TiC electrodes before and after test look consistent without the peak related to carbonates or carboxylates, validating the high electrochemical stability of a-MnOx/TiC electrode under OER condition. However, the XRD spectra of after-charging a-MnOx/C electrode present obvious diffraction peaks corresponding to K₂CO₃ and KHCO₃ (Fig. 4f). Combined XRD patterns (Fig. 4f) with SEM/EDS characterization (Fig. 4d) for before- and after-testing a-MnOx/C electrodes, the solid film on electrode surface is identified as K₂CO₃ and KHCO₃. It is concluded that the continuous oxidation of carbon can cause the formation of carbonates which eventually precipitate out from the electrolyte solution and deposit on the surface of a-MnOx/C electrode, leading to reduction in electrolyte conductivity, passivation of active sites and blockage of the pores in
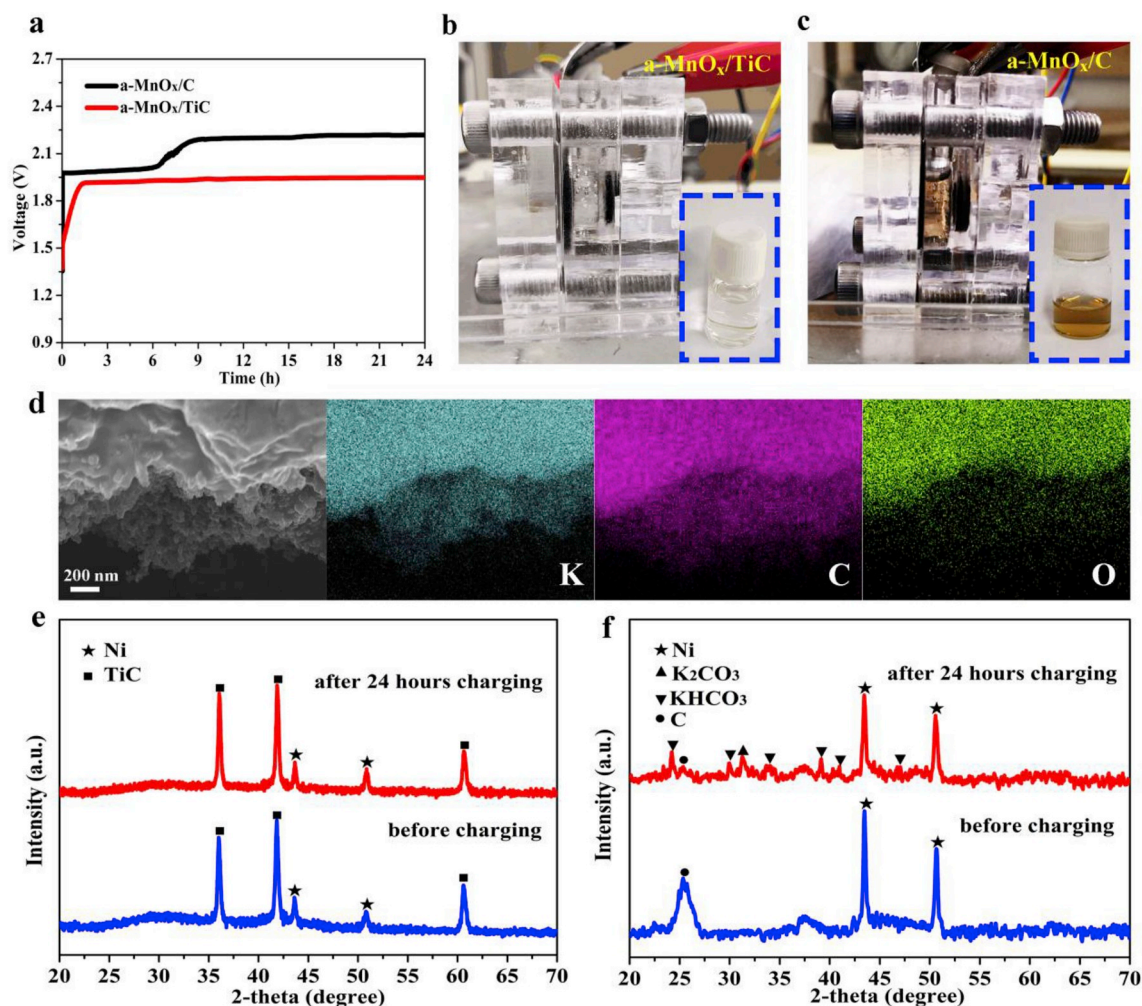
Fig. 4. The charge voltage profile of ZABs in 6 M KOH electrolyte with a-MnO$_x$/TiC and a-MnO$_x$/C oxygen electrodes at 10 mA cm^{-2} for 24 h (a); The home-made ZABs with a-MnO$_x$/TiC (b) and a-MnO$_x$/C (c) after charging for 24 h. The insets in (b) and (c) illustrate the corresponding electrolyte solutions collected from the ZAB in (b) and (c), respectively; SEM image and the corresponding EDS spectra of K, C and O elements (d); XRD patterns of a-MnO$_x$/TiC (e) and a-MnO$_x$/C (f) oxygen electrodes removed from the ZAB in (b) and (c), respectively.
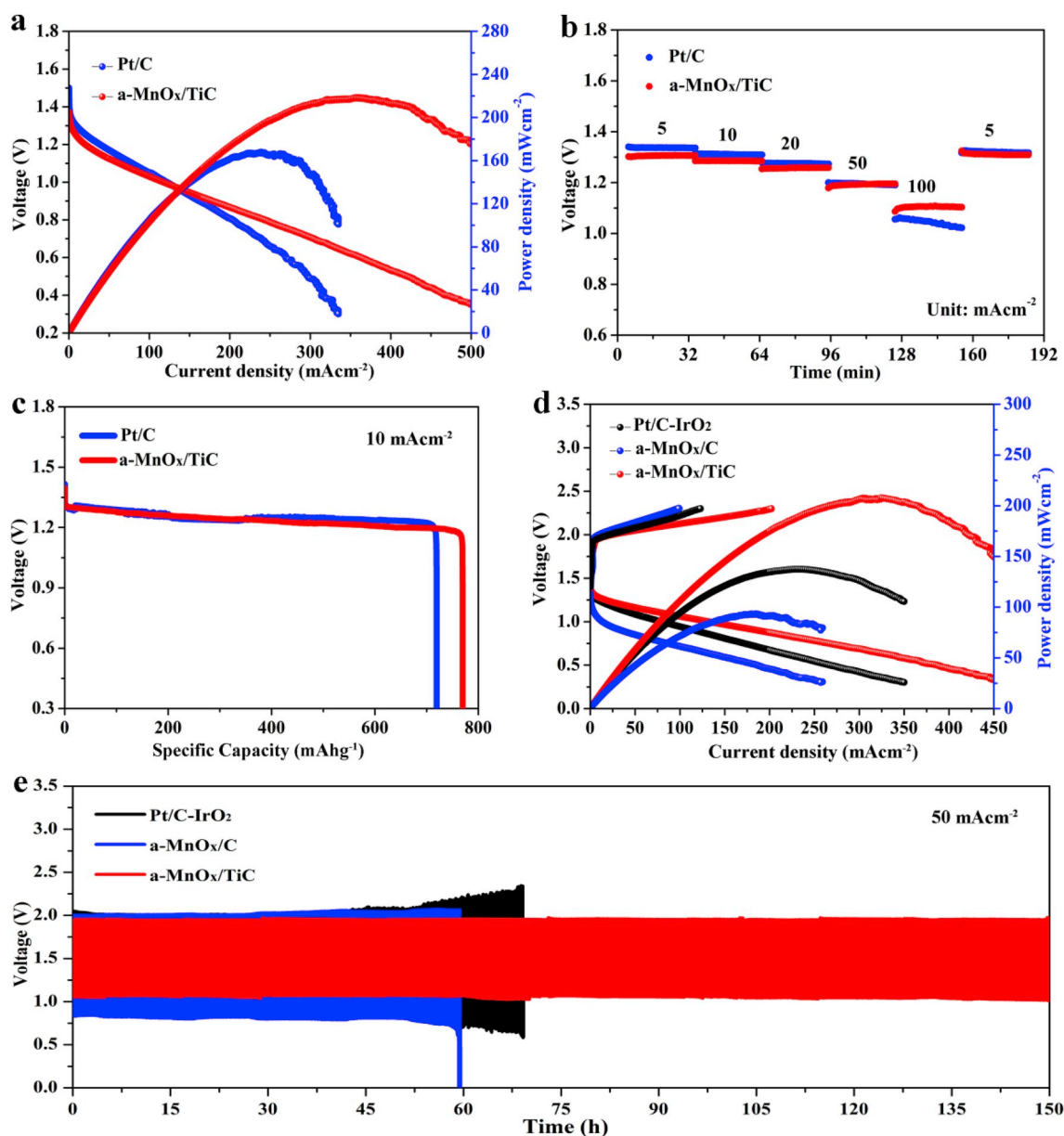
oxygen electrode. A-MnO$_x$/TiC electrode with high chemical and electrochemical stability distinctly demonstrates its potential to serve in rechargeable ZABs with long-term cycling stability.

3.4. Performance of ZABs

On the basis of excellent bifunctional activity and stability of a-MnO$_x$/TiC catalyst, primary and rechargeable home-made ZABs were assembled to assess their practical performance, in which polished zinc plates were used as the anodes and a-MnO$_x$/TiC loaded on stainless steel wire gauzes (1 mg cm^{-2}) served as the cathodes. 6 M KOH and 6 M KOH containing 0.2 M zinc acetate was employed as the electrolyte for primary and rechargeable ZAB, respectively. Pt/C and Pt/C-IrO$_2$ electrodes were prepared with the same method as that for a-MnO$_x$/TiC electrode and performed separately as the reference for primary and rechargeable ZABs. Fig. 5a shows the discharge polarization curves for ZABs with Pt/C and a-MnO$_x$/TiC electrodes. A-MnO$_x$/TiC-based ZAB delivers a peak power density as high as 217.1 mW cm^{-2} at 0.6 V, much greater than that of ZAB with Pt/C (164.8 mW cm^{-2}). When compared with other state-of-the art works (Table S2), this discharge performance of ZAB with a-MnO$_x$/TiC is among the highest ones ever reported. It can be seen that under the current density lower than 100 mA cm^{-2}, Pt/C slightly surpasses a-MnO$_x$/TiC in discharge voltages, in accordance with the ORR activity shown in Fig. 3a. However, above 100 mA cm^{-2}, Pt/C presents

rapid performance decay, from 1.05 V @ 100 mA cm^{-2} to 0.3 V @ 335 mA cm^{-2}. In contrast, a-MnO$_x$/TiC can still sustain a high discharge voltage of 0.65 V @ 335 mA cm^{-2}, which is more than twice of that for Pt/C, indicating an excellent discharge stability and high-rate discharge capability. Due to the difference in electronic structures, the interaction between Pt catalyst and carbon support is relatively weak [53], which may readily cause the migration and aggregation of Pt NPs and the loss of active sites during discharge process, especially for the case under high current densities. On the other hand, the carbon material with large SSA may undergo the chemical attack from active oxygen species (O*, OH*, OOH*) during ORR, resulting the loss of Pt catalyst as well. This corrosion behavior may become severe at higher current density as the formation speed and concentration of the oxygen species correspondingly get higher. The rate performance of ZABs were investigated by galvanostatic measurements for 30 min at various current densities from 5 to 100 mA cm^{-2} and eventually back to 5 mA cm^{-2}. As shown in Fig. 5b, a-MnO$_x$/TiC-based ZAB exhibits consistent discharge voltage plateaus at each current density applied, maintaining 1.1 V even at a high current density of 100 mA cm^{-2}. Once the current density turns back to 5 mA cm^{-2}, the discharge voltage can be fully reproduced to reach that (1.30 V) tested at the previous 5 mA cm^{-2}. Furthermore, a-MnO$_x$/TiC shows comparable performance to Pt/C at low current densities from 5 to 50 mA cm^{-2}. Nevertheless, at 100 mA cm^{-2}, Pt/C delivers significantly lower voltage than its a-MnO$_x$/TiC counterpart and an obvious voltage

Fig. 5. Performance of primary ZABs in 6 M KOH electrolyte with Pt/C and a-MnOx/TiC oxygen electrodes. Discharge polarization curves and the corresponding power densities (a), rate performance from 5 to 100 mA cm^{-2} (b), and specific pristine capacities at 10 mA cm^{-2} (c); Performance of rechargeable ZABs in 6 M KOH with 0.2 M Zn(Ac)$_2$ mixed electrolyte with Pt/C-IrO$_2$, a-MnOx/C and a-MnOx/TiC oxygen electrodes. Charge/discharge polarization curves (d), cycle tests at 50 mA cm^{-2} (e).

drop during the galvanostatic process, confirming the poor rate performance of Pt/C at high current density, which has also been reported in some literatures on fuel cells [54] or ZABs [55]. The discharge voltage for ZAB with Pt/C reduces from 1.33 V to 1.31 V when the current density returns to 5 mA cm^{-2}, suggesting a performance degradation of Pt/C oxygen electrode after a short-term galvanostatic measurement. The synergistic effect of a-MnO$_x$ and TiC is regarded to account for the high and stable discharge performance of a-MnO$_x$/TiC-based ZAB. The stable TiC substrate and well-anchored a-MnO$_x$ NPs are conducive to retaining the active sites during ORR process. Based on the mass of zinc, ZABs using Pt/C and a-MnO$_x$/TiC deliver the specific capacities of 719.3 and 769.8 mAh g^{-1}, respectively at 10 mA cm^{-2}, of which the latter specific capacity is 93.8% of the theoretical value (820 mAh g^{-1}), as shown in Fig. 5c. The relatively low durability of Pt/C probably confines the capacity delivery of Zn electrode.

A-MnO$_x$/TiC was further evaluated on the bifunctional activity in

rechargeable ZABs using 6 M KOH containing 0.2 M zinc acetate as the electrolyte, compared with the commonly used bifunctional catalyst of Pt/C-IrO$_2$ (1:1 in mass ratio) and the a-MnO$_x$/C counterpart. All the ZABs possess similar impedance behavior in Fig. S12 with the ohmic resistance of 2.0 Ω cm^2, suggesting their similar internal resistance and the consistent fabrication process. Fig. 5d shows that the rechargeable ZAB with a-MnO$_x$/TiC still delivers a superior maximum power density of 207.6 mA cm^{-2} at 0.7 V to that of Pt/C-IrO$_2$-based ZAB (137.4 mW cm^{-2} @ 0.58 V) and a-MnO$_x$/C-based ZAB (93.2 mW cm^{-2} @ 0.5 V). The overpotentials for both the discharge and charge processes for ZAB with a-MnO$_x$/TiC are remarkably lower than those of the benchmark Pt/C-IrO$_2$-based ZAB. It may be not surprised at the superior bifunctional activity of a-MnO$_x$/TiC since it shows a smaller potential gap (ΔE) than the value calculated from Pt/C and IrO$_2$ in Fig. 3i. Given that Pt/C and IrO$_2$ separately facilitate ORR and OER, it is speculated that there may lack efficient synergistic effect between Pt/C and IrO$_2$ at least for this

simply mixed Pt/C-IrO$_2$ hybrid catalyst. It demonstrates that the synergistic effect, durability and stability of catalysts during ORR and OER play vital roles in addition to the ORR/OER activity revealed in RDE measurements. The cycle performances of ZABs with Pt/C-IrO$_2$, a-MnO$_x$/C and a-MnO$_x$/TiC oxygen electrodes were tested at 50 mA cm^{-2} using different capacity limited protocols. In Fig. 5e, a-MnO$_x$/TiC-based ZAB shows a ultra consistent and high stability under the cycling protocol of 5 min-discharge followed by 5 min-charge at 50 mA cm^{-2} for 150 h until the battery is voluntarily terminated. The discharge voltage changes from 1.05 to 1.01 V and charge voltage varies from 1.953 to 1.955 V during cycling, presenting the voltage gap of only 0.9 V. In contrast, ZAB with Pt/C-IrO$_2$ and a-MnO$_x$/C are far behind, either in cycle performance or stability. The battery with Pt/C-IrO$_2$ can be only cycled for 69 h with a fast performance fading, demonstrating a low durability of Pt/C-IrO$_2$ catalyst. The a-MnO$_x$/C-based ZAB exhibits the poorest cycling performance with the lowest discharge voltage and eventually died after only 58-hrs-cycling. Again, in Table S2 it demonstrates that the cycling stability of a-MnO$_x$/TiC-based ZAB is among the best results in previous literature reports. The ZABs with Pt/C-IrO$_2$ and a-MnO$_x$/TiC were further cycled at 70 mA cm^{-2} under a relatively slow cycling protocol of 30 min-discharge followed by 30 min-charge, as

shown in Fig. S13. Again, ZAB with a-MnO$_x$/TiC delivers an outstanding cycle performance with high stability and round-trip efficiency, markedly outperforming Pt/C-IrO$_2$-based ZAB. These results further validate the superior discharge/charge cycling performance of a-MnO$_x$/TiC to that of Pt/C-IrO$_2$, attributing to the high stability and activity of a-MnO$_x$/TiC for ORR and OER.

Solid-state Zn-air coin cells and the flexible batteries are fabricated to verify the potential application for portable and wearable electronics. Fig. 6a illustrates the configuration of a solid-state Zn-air coin cell, displaying the flexible a-MnO$_x$/TiC oxygen electrode (1), flexible solid-state electrolyte (2), Zn chip anode (3) and the assembled coin cell (4). The Zn-air coin cell delivers a relatively high discharge performance with a peak power density of 63 mW cm^{-2} (Fig. 6b), and a stably discharge and charge cycling performance for 24 h with a low voltage gap of only 0.12 V (Fig. 6c). Furthermore, this coin cell shows excellent durability with a consistently stable charge voltage of 1.4 V and a discharge voltage of 1.28 V without obvious performance fading, which can be attributed to the superior ORR/OER bifunctional activity and stability of corrosion resistant a-MnO$_x$/TiC oxygen electrode. The open circuit voltage (OCV) for a SSZAB is 1.356 V in Fig. 6d. As a demonstration, two series connected SSZABs shows capability of powering an
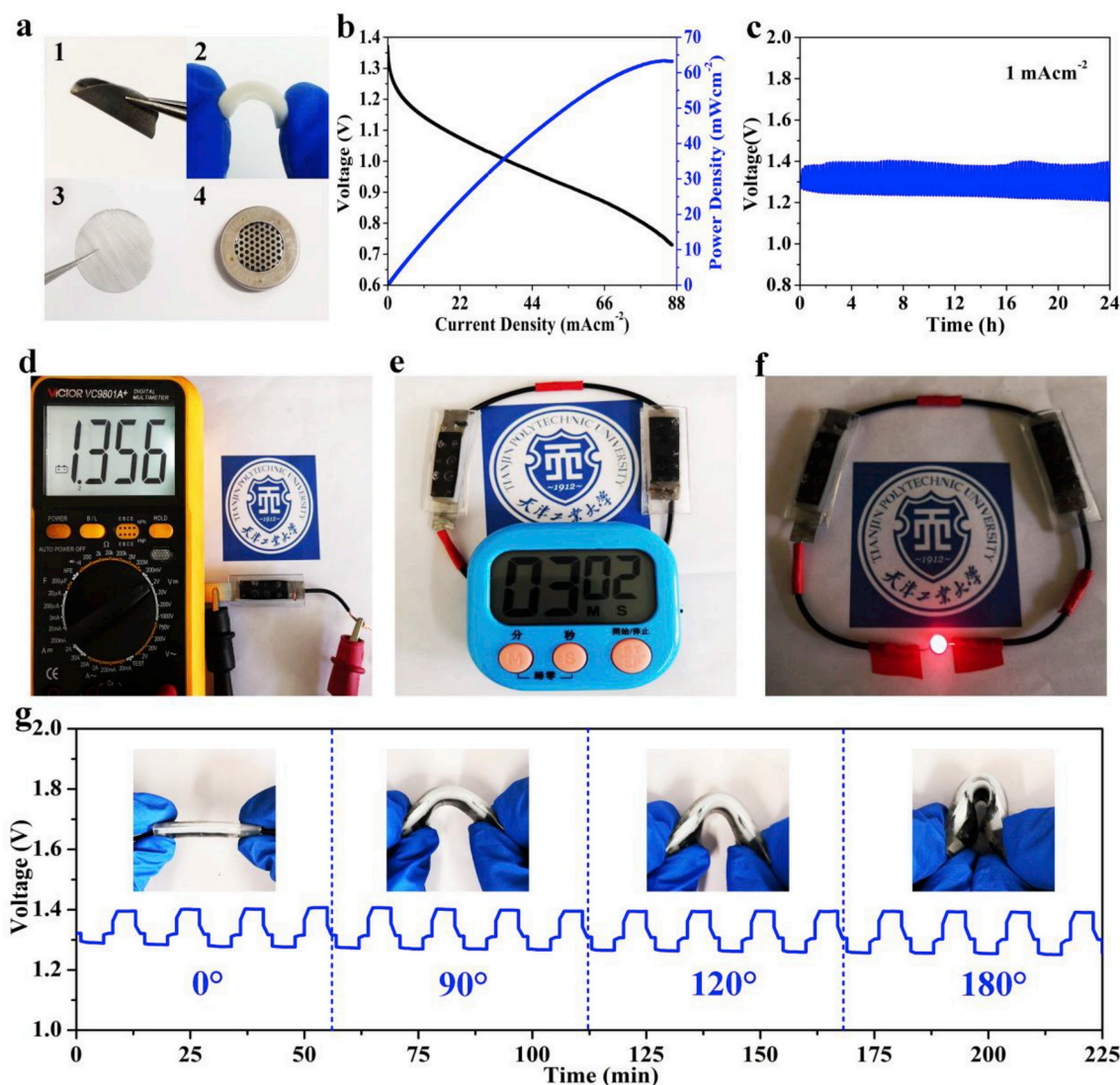
Fig. 6. Digital images of the solid-state Zn-air coin cell and its configuration (a), comprising the flexible a-MnOx/TiC oxygen electrode (1), flexible solid-state electrolyte (2), Zn electrode (3) and the assembled coin cell (4); Discharge polarization curve and the corresponding power density (b) and the cycle performance at 1 mA cm-2 (c) of the solid-state Zn-air coin cell; Digital images of foldable SSZABs showing open circuit potential (d), powering the electronic watch (e) and a red LED (f); Cycle performance of the SSZAB at 1 mA cm-2 at flat and bent states under various angles (g).

electronic watch and a red LED, as shown in Fig. 6e and f, respectively. Fig. S14 shows the photos for SSZABs under bending state, which demonstrate similar performances as those presented in Fig. 6d–f, manifesting great perspective for their application in small portable electronics. To further examine the flexible nature and cycling stability of SSZAB, it was galvanostatically cycled at $1 \, mA \, cm^{-2}$ alongside folding under different bending angles from its flat ($0°$) to folded ($180°$) states for every four cycles, as shown in the insets in Fig. 6g. During the cycles with large structural changes, the SSZAB exhibits stable charge ($1.4 \, V$) and discharge ($1.25 \, V$) voltages, indicating the a-MnO_x/TiC-based SSZAB possesses robust flexibility and cycle stability to against the impact of mechanical deformation on battery performance. As demonstrated above, the SSZAB with a-$MnOx$/TiC can be promising energy storage systems with high efficiency and durability for portable and wearable electronics.

4. Conclusions

In summary, a corrosion resistant bifunctional electrocatalyst composed of amorphous MnO_x nanoparticles on TiC support was successfully prepared for rechargeable Zn-air batteries. The obtained a-MnO_x/TiC exhibits a remarkably high catalytic activity and stability for both ORR and OER, far surpassing the commercial catalyst of Pt/C, IrO_2, Pt/C-IrO_2 hybrid, as well as its a-MnO_x/C counterpart. The excellent electrocatalytic activity of a-MnO_x/TiC can be attributed to the efficient synergistic effect which provides sufficient active sites for O_2 adsorption/desorption, rich Mn^{III} and Mn^{IV} ions to facilitate charge transfer process for ORR and OER, and fast electron transfer. Furthermore, a-MnO_x/TiC demonstrates a superior corrosion-resistive capability in strong alkaline electrolyte under OER condition to the readily oxidized carbon-based catalysts, owing to its high chemical and electrochemical stability over carbon-based materials. The liquid ZAB with a-MnO_x/TiC delivers a high discharge performance especially at high current densities, with a peak power density of $217.1 \, mW \, cm^{-2}$, much greater than that of ZAB with Pt/C ($164.8 \, mW \, cm^{-2}$). Besides, the a-MnO_x/TiC-based ZAB exhibits superior cycling performance and stability, far overwhelming the ZABs with Pt/C-IrO_2 and a-MnO_x/C, presenting a consistently low voltage gap of only $0.9 \, V$. Additionally, solid-state ZAB using a-MnO_x/TiC demonstrates excellent mechanical flexibility and cycle stability under its flat and bent states. The corrosion resistant a-MnO_x/TiC bifunctional electrocatalyst with superior activity and durability provides a very promising strategy for accelerating the practical application of reliable Zn-air batteries for portable electronics and electric vehicles.

Declaration of competing interest

The authors declare that they have no known competing financial interests or personal relationships that could have appeared to influence the work reported in this paper.

Acknowledgement

Appendix A. Supplementary data

Supplementary data to this article can be found online at https://doi.org/10.1016/j.nanoen.2019.104208.

References

[1] Z.P. Cano, D. Banham, S. Ye, A. Hintennach, J. Lu, M. Fowler, Z. Chen, Batteries and fuel cells for emerging electric vehicle markets, Nat. Energy. 3 (2018) 279–289.

[2] C.J. Wook, A. Doron, Promise and reality of post-lithium-ion batteries with high energy densities, Nat. Rev. Mater. 1 (2016) 16013.

[3] J. Cabana, L. Monconduit, D. Larcher, Beyond intercalation-based Li-ion batteries: the state of the art and challenges of electrode materials reacting through conversion reactions, Adv. Mater. 22 (2010) 170–192.

[4] P. Gu, M. Zheng, Q. Zhao, X. Xiao, H. Xue, H. Pang, Rechargeable zinc-air batteries: a promising way to green energy, J. Mater. Chem. A. 5 (2017) 7651–7666.

[5] P.G. Bruce, S.A. Freunberger, L.J. Hardwick, J.M. Tarascon, Li-O2 and Li-S batteries with high energy storage, Nat. Mater. 11 (2011) 19–29.

[6] J. Fu, R. Liang, G. Liu, A. Yu, Z. Bai, L. Yang, Z. Chen, Recent progress in electrically rechargeable zinc-air batteries, Adv. Mater. (2018) 1805230.

[7] J. Pan, Y.Y. Xu, H. Yang, Z. Dong, H. Liu, B.Y. Xia, Advanced architectures and relatives of air electrodes in Zn-air batteries, Adv. Sci. 5 (2018) 1700691.

[8] J.S. Lee, S.T. Kim, R. Cao, N.S. Choi, M. Liu, K.T. Lee, J. Cho, Metal-air batteries with high energy density: Li-Air versus Zn-Air, Adv. Energy Mater. 1 (2011) 34–50.

[9] V. Caramia, B. Bozzini, Materials science aspects of zinc-air batteries: a review, Mater. Renew. Sustain. Energy 3 (2014) 28.

[10] Y. Li, C. Zhong, J. Liu, X. Zeng, S. Qu, X. Han, Y. Deng, W. Hu, J. Lu, Atomically thin mesoporous Co3O4 layers strongly coupled with N-rGO nanosheets as high-performance bifunctional catalysts for 1D knittable zinc-air batteries, Adv. Mater. 30 (2018) 1703657.

[11] L. Ma, S. Chen, D. Wang, Q. Yang, F. Mo, G. Liang, N. Li, H. Zhang, J.A. Zapien, C. Zhi, Super-stretchable zinc-air batteries based on an alkaline-tolerant dual-network hydrogel electrolyte, Adv. Energy Mater. (2019) 1803046.

[12] G. Fu, Z. Cui, Y. Chen, L. Xu, Y. Tang, J.B. Goodenough, Hierarchically mesoporous nickel-iron nitride as a cost-efficient and highly durable electrocatalyst for Zn-air battery, Nano Energy 39 (2017) 77–85.

[13] J. Han, X. Meng, L. Lu, J. Bian, Z. Li, C. Sun, Single-atom Fe-Nx-C as an efficient electrocatalyst for zinc-air batteries, Adv. Funct. Mater. (2019) 1808872.

[14] D.U. Lee, P. Xu, Z.P. Cano, A.G. Kashkooli, M.G. Park, Z. Chen, Recent progress and perspectives on bifunctional oxygen electrocatalysts for advanced rechargeable metal-air batteries, J. Mater. Chem. A. 4 (2016) 7107–7134.

[15] Y. Guo, P. Yuan, J. Zhang, H. Xia, F. Cheng, M. Zhou, J. Li, Y. Qiao, S. Mu, Q. Xu, Co2P-CoN double active centers confined in N-Doped carbon nanotube: heterostructural engineering for trifunctional catalysis toward HER, ORR, OER, and Zn-Air batteries driven water splitting, Adv. Funct. Mater. 28 (2018) 1805641.

[16] Y. Guo, P. Yuan, J. Zhang, Y. Hu, I.S. Amiinu, X. Wang, J. Zhou, H. Xia, Z. Song, Q. Xu, S. Mu, Carbon nanosheets containing discrete Co-Nx-By-C active sites for efficient oxygen electrocatalysis and rechargeable Zn-air batteries, ACS Nano 12 (2018) 1894–1901.

[17] P. Chen, T. Zhou, L. Xing, K. Xu, Y. Tong, H. Xie, L. Zhang, W. Yan, W. Chu, C. Wu, Atomically dispersed iron-nitrogen species as electrocatalysts for bifunctional oxygen evolution and reduction reactions, Angew. Chem. Int. Ed. 56 (2017) 610–614.

[18] K. Gong, F. Du, Z. Xia, M. Durstock, L. Dai, Nitrogen-doped carbon nanotube arrays with high electrocatalytic activity for oxygen reduction, Science 323 (2009) 760–764.

[19] X. Chen, L. Yu, S. Wang, D. Deng, X. Bao, Highly active and stable single iron site confined in graphene nanosheets for oxygen reduction reaction, Nano Energy 32 (2017) 353–358.

[20] S. Gupta, W. Kellogg, H. Xu, X. Liu, J. Cho, G. Wu, Bifunctional perovskite oxide catalysts for oxygen reduction and evolution in alkaline media, Chem. Asian J. 11 (2016) 10–21.

[21] H.H. Cheng, C.S. Tan, Reduction of CO2 concentration in a zinc/air battery by absorption in a rotating packed bed, J. Power Sources 162 (2006) 1431–1436.

[22] N. Xu, Y. Zhang, T. Zhang, Y. Liu, J. Qiao, Efficient quantum dots anchored nanocomposite for highly active ORR/OER electrocatalyst of advanced metal-air batteries, Nano Energy 57 (2019) 176–185.

[23] R. Li, Z. Wei, X. Gou, Nitrogen and phosphorus dual-doped graphene/carbon nanosheets as bifunctional electrocatalysts for oxygen reduction and evolution, ACS Catal. 5 (2015) 4133–4142.

[24] F. Cheng, J. Shen, B. Peng, Y. Pan, Z. Tao, J. Chen, Rapid room-temperature synthesis of nanocrystalline spinels as oxygen reduction and evolution electrocatalysts, Nat. Chem. 3 (2011) 79–84.

[25] B. Zhao, L. Zhang, D. Zhen, S. Yoo, Y. Ding, D. Chen, Y. Chen, Q. Zhang, B. Doyle, X. Xiong, A tailored double perovskite nanofiber catalyst enables ultrafast oxygen evolution, Nat. Commun. 8 (2017) 14586.

[26] T. Ling, D. Yan, Y. Jiao, H. Wang, Y. Zheng, X. Zheng, J. Mao, X. Du, Z. Hu, M. Jaroniec, S. Qiao, Engineering surface atomic structure of single-crystal cobalt (II) oxide nanorods for superior electrocatalysis, Nat. Commun. 7 (2016) 12876.

[27] A. Sumboja, M. Lübke, Y. Wang, T. An, Y. Zong, Z. Liu, All-solid-state, foldable, and rechargeable Zn-air batteries based on manganese oxide grown on graphene-coated carbon cloth air cathode, Adv. Energy Mater. 7 (2017) 1700927.

[28] Y. Meng, W. Song, H. Huang, Z. Ren, S. Chen, S.L. Suib, Structure-property relationship of bifunctional MnO2 nanostructures: highly efficient, ultra-stable electrochemical water oxidation and oxygen reduction reaction catalysts identified in alkaline media, J. Am. Chem. Soc. 136 (2014) 11452–11464.

[29] D.M. Robinson, Y.B. Go, M. Mui, Photochemical water oxidation by crystalline polymorphs of manganese oxides: structural requirements for catalysis, J. Am. Chem. Soc. 135 (2013) 3494–3501.

[30] I. Roche, E. Chaînet, M. Chatenet, Carbon-supported manganese oxide nanoparticles as electrocatalysts for the oxygen reduction reaction (ORR) in alkaline medium: physical characterizations and ORR mechanism, J. Phys. Chem. C 111 (2007) 1434–1443.

[31] Q. Tang, L. Jiang, J. Liu, S. Wang, G. Sun, Effect of surface manganese valence of manganese oxides on the activity of the oxygen reduction reaction in alkaline media, ACS Catal. 4 (2014) 457–463.

[32] J.S. Lee, G.S. Park, H.I. Lee, S.T. Kim, R.G. Cao, M.L. Liu, J. Cho, Ketjenblack carbon supported amorphous manganese oxides nanowires as highly efficient electrocatalyst for oxygen reduction reaction in alkaline solutions, Nano Lett. 11 (2011) 5362–5366.

[33] Y. Zhong, X. Xia, F. Shi, J. Zhan, J. Tu, H. Fan, Transition metal carbides and nitrides in energy storage and conversion, Adv. Sci. 3 (2016) 1500286.

[34] Z. Qiu, H. Huang, J. Du, X. Tao, Y. Xia, T. Feng, Y. Gan, W. Zhang, Biotemplated synthesis of bark-structured TiC nanowires as Pt catalyst supports with enhanced electrocatalytic activity and durability for methanol oxidation, J. Mater. Chem. A. 2 (2014) 8003–8008.

[35] L. Liao, X. Bian, J. Xiao, B. Liu, M.D. Scanlonb, H.H. Girault, Nanoporous molybdenum carbide wires as an active electrocatalyst towards the oxygen reduction reaction, Phys. Chem. Chem. Phys. 16 (2014) 10088–10094.

[36] Y. Chen, X. Zhang, H. Cui, X. Zhang, Z. Xie, X. Wang, M. Jiao, Z. Zhou, Synergistic electrocatalytic oxygen reduction reactions of Pd/B$_4$C for ultrastable Zn-air batteries, Energy Storage Mater. 15 (2018) 226–233.

[37] S. Song, W. Xu, R. Cao, L. Luo, M.H. Engelhard, M.E. Bowden, B. Liu, L. Estevez, C. Wang, J. Zhang, B$_4$C as a stable non-carbon-based oxygen electrode material for lithium-oxygen batteries, Nano Energy 33 (2017) 195–204.

[38] Y. Weng, N. Wu, Titanium carbide@polypyrrole core-shell nanoparticles prepared by controlled heterogeneous nucleation for rechargeable batteries, Chem. Commun. 49 (2013) 10784–10786.

[39] M.M.O. Thotiyl, S.A. Freunberger, Z. Peng, Y. Chen, Z. Liu, P.G. Bruce, A stable cathode for the aprotic Li-O$_2$ battery, Nat. Mater. 11 (2013) 1049–1055.

[40] Q. Xue, Z. Pei, Y. Huang, M. Zhu, Z. Tang, H. Li, Y. Huang, N. Li, H. Zhang, C. Zhi, Mn$_3$O$_4$ nanoparticles on layer-structured Ti$_3$C$_2$ MXene towards oxygen reduction reaction and zinc-air battery, J. Mater. Chem. A. 10 (2017) 20818–20823.

[41] T. Ma, J. Cao, M. Jaroniec, S. Qiao, Interacting carbon nitride and titanium carbide nanosheets for high-performance oxygen evolution, Angew. Chem. 128 (2016) 1150–1154.

[42] J. Kang, H. Wang, S. Ji, J. Key, R. Wang, Synergistic among manganese, nitrogen and carbon to improve the catalytic activity for oxygen reduction reaction, J. Power Sources 251 (2014) 363–369.

[43] J. Pandey, B. Hu, W. Ng, Y. Yang, K. van der Veen, J. Chen, N.J. Geels, J. Luo, G. Rothenberg, N. Yan, Developing hierarchically porous MnO$_x$/NC hybrid nanorods for oxygen reduction and evolution catalysis, Green Chem. 19 (2017) 2793–2797.

[44] M. Piumetti, D. Fino, N. Russo, Mesoporous manganese oxides prepared by solution combustion synthesis as catalysts for the total oxidation of VOCs, Appl. Catal., B 163 (2015) 277–287.

[45] H. Li, X. Li, J. Liang, Y. Chen, Hydrous RuO$_2$-decorated MXene coordinating with silver nanowire inks enabling fully printed micro-supercapacitors with extraordinary volumetric performance, Adv. Energy Mater. 9 (2018) 1803987.

[46] W. Yang, Z. Su, Z. Xua, W. Yang, Y. Peng, J. Li, Comparative study of α-, β-, γ- and δ-MnO$_2$ on toluene oxidation: oxygen vacancies and reaction intermediates, Appl. Catal. B Environ. 260 (2020) 118150.

[47] L. Laffonta, P. Gibot, High resolution electron energy loss spectroscopy of manganese oxides: application to Mn$_3$O$_4$ nanoparticles, Mater. Char. 61 (2010) 1268–1273.

[48] M. Minakshi, Examining manganese dioxide electrode in KOH electrolyte using TEM technique, J. Electroanal. Chem. 616 (2008) 99–106.

[49] J.E. Oghenevwetaa, D. Wexler, A. Calka, Study of reaction sequences during MSR synthesis of TiC by controlled ball milling of titanium and graphite, Mater. Char. 140 (2018) 299–311.

[50] E. Stoyanov, F. Langenhorst, G. Steinle-Neumann, The effect of valence state and site geometry on Ti L$_{3,2}$ and O K electron-energy-loss spectra of Ti$_x$O$_y$ phases, Am. Mineral. 92 (2007) 577–586.

[51] B.H. Lohse, A. Calka, D. Wexler, Raman spectroscopy as a tool to study TiC formation during controlled ball milling, J. Appl. Phys. 97 (2005) 114912.

[52] a) P.N. Ross, H. Sokol, The corrosion of carbon black anodes in alkaline electrolyte I. Acetylene black and the effect of cobalt catalyzation, J. Electrochem. Soc. 131 (1984) 1742–1750;
b) H. Arai, S. Müller, O. Haas, AC impedance analysis of bifunctional air electrodes for metal-air batteries, J. Electrochem. Soc. 147 (2000) 3584–3591;
c) A. Sumboja, X. Ge, G. Zheng, F.W.T. Goh, T.S.A. Hor, Y. Zong, Z. Liu, Durable rechargeable zinc-air batteries with neutral electrolyte and manganese oxide catalyst, J. Power Sources 332 (2016) 330–336.

[53] L. Li, L. Hu, J. Li, Enhanced stability of Pt nanoparticle electrocatalysts for fuel cells, Nano Res. 8 (2015) 418–440.

[54] X. Xie, S. Chen, W. Ding, Y. Nie, Z. Wei, An extraordinarily stable catalyst: Pt NPs supported on two-dimensional Ti$_3$C$_2$X$_2$ (X = OH, F) nanosheets for oxygen reduction reaction, Chem. Commun. 49 (2013) 10112–10114.

[55] S. Liu, M. Wang, X. Sun, N. Xu, J. Liu, Y. Wang, T. Qian, C. Yan, Facilitated oxygen chemisorption in heteroatom-doped carbon for improved oxygen reaction activity in all-solid-state zinc-air batteries, Adv. Mater. 4 (2018) 1704898.

Shidong Song is currently a full professor at the school of Chemistry and Chemical Engineering at Tianjin Polytechnic University (TJPU), China. He received his B.S. and M.S. from Nankai University and earned his Ph.D. in Electrochemical Engineering from Tianjin University in 2004. Then he carried out research at Kyushu University (Japan) and University of St. Andrews (UK) as a postdoc and PNNL (USA) as an ASF. His research interest mainly focuses on nano-functional materials for energy conversion and storage, including metal-air batteries and fuel cells.
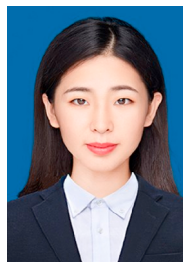
Wanjun Li received her Bachelor degree from Shenyang University of Technology of China in 2017. Currently, she is working on her Master Degree in chemical engineering with Prof. Shidong Song at Tianjin Polytechnic University (TJPU). Her research focuses on high-performance and high-stability electrocatalysts for electrochemical energy storage applications such as metal-air batteries.

Ya-Ping Deng received his Master's degree (2016) in Xiamen University with Prof. Shi-Gang Sun. He is now pursuing his Ph. D. in Chemical Engineering under the supervision of Prof. Zhongwei Chen at University of Waterloo. His research currently focusses on the exploration of novel electrode materials and solid–state electrolytes for lithium–ion batteries and rechargeable metal–air batteries.

Yanli Ruan received her Ph.D. in Applied Chemistry from Tianjin University in 2006. She is currently a full professor at the school of Chemistry and Chemical Engineering at Tianjin Polytechnic University (TJPU), China. In 2016, She worked at LBNL (USA) on high-performance lithium (sodium) batteries as a visiting scholar. Her research interest mainly focuses on novel nano-structure materials for energy storage and conversion systems.

Yining Zhang received his PH.D. in Chemical Engineering from Dalian Institute of Chemical Physics, Chinese Academy of Sciences in 2010. He is currently a post-doctoral research fellow in University of Waterloo, Canada. His research interests mainly focus on energy storage and conversion techniques, including fuel cells, metal-air batteries, lithium batteries, flow batteries etc.

Xuhui Qin received his Bachelor degree from Tianjin Poly-technic University (TJPU) of China in 2017. Currently, he is working on his Master Degree in chemical engineering with Prof. Shidong Song at Tianjin Polytechnic University (TJPU). His research focuses on highly conductive and durable solid-state electrolyte materials for solid-state batteries.

Dr. Zhongwei Chen is Canada Research Chair Professor in Advanced Materials for Clean Energy at University of Waterloo, fellow of the Royal Society of Canada and fellow of the Canadian Academy of Engineering. His research interests are in the development of advanced energy materials for metal-air batteries, lithiumion batteries and fuel cells. He has published 1 book, 7 book chapters and more than 300 peer reviewed journal articles with over 20,000 citations with H-index 70 (Google Scholar). He is also listed as inventor on 15 US/international patents, with several licensed to companies in USA and Canada. He was recipient of the 2016 E. W. R Steacie Memorial Fellowship, which followed shortly upon several other prestigious honors, including the Ontario Early Researcher Award, an NSERC Discovery Supplement Award, the Distinguished Performance and the Research Excellence Awards from the University of Waterloo.